



EBSD Study of Microstructural and Textural Changes of Hot-Rolled Ti–6Al–4V Sheet After Annealing at 800 °C

Ji-Ying Xia¹ · Lin-Jiang Chai¹ · Hao Wu¹ · Yan Zhi¹ · Yin-Ning Gou¹ · Wei-Jiu Huang¹ · Ning Guo²

Received: 21 March 2018 / Revised: 28 April 2018 / Published online: 26 June 2018
© The Chinese Society for Metals and Springer-Verlag GmbH Germany, part of Springer Nature 2018

Abstract

In this paper, electron backscatter diffraction and various other characterization and analysis techniques including X-ray diffraction, electron channeling contrast imaging and energy-dispersive spectrometry were jointly employed to investigate microstructural and textural changes of a hot-rolled Ti–6Al–4V (TC4) sheet after annealing at 800 °C for 5 h. In addition, the hardness variation induced by the annealing treatment is rationalized based on revealed microstructural and textural characteristics. Results show that the TC4 sheet presents a typical dual-phase ($\alpha + \beta$) microstructure, with α -Ti as the major phase and short-rod-shaped β -Ti (minority) uniformly distributed throughout the α matrix. Most of α grains correspond to the un-recrystallized structures with a typical rolling texture ($c//TD$ and $\langle 11\text{--}20 \rangle // ND$) and dense low angle boundaries (LABs). After the annealing, the stored energy in the as-received specimen is significantly reduced, along with greatly decreased LABs density. Also, the annealing allows recrystallization and grain growth to occur, leading to weakening of the initial texture. Furthermore, the water quenching immediately after the annealing triggers martensitic transformation, which makes the high-temperature β phases be transformed into submicron α plates. The hardness of the annealed specimen is 320.5 HV, lower than that (367.0 HV) of the as-received specimen, which could be attributed to reduced LABs, grain growth and weakened texture. Nevertheless, the hardening effect from the fine martensitic plates could help to suppress a drastic hardness drop.

Keywords Ti alloy · Electron backscatter diffraction · Recrystallization · Texture · Hardness

1 Introduction

Due to many attractive properties like good corrosion resistance, low density and high strength-to-weight ratio, Ti and its alloys have important engineering applications in aerospace, automotive, petrochemical and biomedical industries [1–5]. Among them, Ti–6Al–4V (TC4) is known

to be the most widely used material and with a typical dual-phase ($\alpha + \beta$) microstructure [2]. After appropriate processings, TC4 alloy could possess excellent comprehensive mechanical properties, which are closely related to their specific microstructures (morphologies, distributions and sizes of both α and β phases) and textures [6, 7]. In order to reach controllable performance for the TC4 alloy, numerous attempts have been stimulated to understand the underlying relationship among mechanical properties and microstructural and textural characteristics developed during various processings [7–14]. For example, Guo et al. [10] investigated influences of annealing at 930–975 °C on the morphologies and sizes of α and β phases in a TC4 alloy and how they affected its strength, plasticity and fracture toughness. Lütjering [11] carried out a systematic study on correlation between the microstructure (especially sizes of both α and β phases) and mechanical properties of TC4 alloys subjected to various thermo-mechanical processings.

Available online at <http://link.springer.com/journal/40195>

- ✉ Lin-Jiang Chai
chailinjiang@cqut.edu.cn
- ✉ Yan Zhi
zhiyan1202@cqut.edu.cn
- ✉ Ning Guo
guoning_1000@163.com

¹ College of Materials Science and Engineering, Chongqing University of Technology, Chongqing 400054, China

² Faculty of Materials and Energy, Southwest University, Chongqing 400715, China

In spite of a considerable amount of knowledge accumulated for TC4 materials, it is to be noted that there is still a lack of clear understanding on their microstructural and textural characteristics after annealing in dual-phase ($\alpha + \beta$) regions. In this case, recrystallization and/or grain growth may occur for the major phase (α -Ti) through migration of high angle boundaries (HABs) along with texture modifications [15]. In the meantime, the high-temperature annealing can also lead to composition variation of the metastable β phase, which may become unstable and then transform into α phase during subsequent cooling [16–19]. In-depth and detailed investigations on such microstructural and textural characteristics should be able to shed some light on optimizing heat treatment regimes for the dual-phase Ti alloy.

In the present work, therefore, multiple analysis techniques (especially electron backscatter diffraction (EBSD)) were jointly employed to characterize microstructures and textures of a hot-rolled TC4 sheet after $\alpha + \beta$ region annealing at 800 °C. After that, the reasons accounting for the annealing-associated microstructural and textural changes were well analyzed with their effects on specimen hardness tentatively explored as well.

2 Experimental

The as-received material was a hot-rolled TC4 alloy sheet (3 mm in thickness), with its chemical composition listed in Table 1. Specimens with the dimension of 10 mm \times 8 mm \times 3 mm in rolling, transverse and normal directions (denoted as RD, TD and ND, respectively) were cut from the as-received sheet. They were sealed into quartz tube under vacuum before annealing to avoid oxidation during heating. The sealed specimens were then heat-treated in a programmable box furnace (SX-G07103) at 800 °C for 5 h before quenching into cold water with an estimated cooling rate of 200 °C/s [20].

Microstructures of the specimens before and after the annealing were mainly characterized by EBSD and electron channeling contrast (ECC) imaging techniques in a Zeiss SIGMA HD field emission gun scanning electron microscope (FEG-SEM). The EBSD system was comprised of a NordlysMax² detector (Oxford Instruments) with AZtec 2.4 and HKL Channel 5 software packages used for data acquisition and post-processing analyses, respectively.

Table 1 Chemical composition of the experimental material (wt%)

Al	V	Fe	C	N	H	O	Ti
6.10	3.98	0.21	0.011	0.027	0.05	0.12	Bal.

An energy-dispersive spectrometer (EDS) attached to the FEG-SEM was also utilized to perform local composition measurements corresponding to specific microstructures. Global phase constituents of the specimens were examined by a conventional X-ray diffractometer (PANalytical Empyrean) using Cu $K\alpha$. Before these examinations, the surfaces of the specimens (RD–TD plane for X-ray diffraction (XRD) and RD–ND plane for ECC and EBSD) were mechanically ground using SiC abrasive paper (3000 # in the final step) and then electro-polished in a mixed solution of 90 mL methanol and 10 mL perchloric acid (at – 30 °C and 14 V for 100 s). In addition, micro-hardness measurements were performed on RD–TD plane of the specimens using a Vickers indentation tester (HVS-100) at a load of 100 g for 10 s. The micro-hardness of each specimen was determined as the average value of 10 measurements.

3 Results and Discussion

3.1 XRD Patterns

Figure 1 presents the results of the XRD examinations for the as-received and the 800 °C-annealed specimens. It is found that all detected peaks can be indexed by either α -Ti with a hexagonal close packed (hcp) structure or β -Ti with a body-centered cubic (bcc) structure. As shown in Fig. 1, a comparison between peak heights of the two phases reveals a much lower intensity for the β phase than the α phase in the as-received specimen. This clearly suggests a dual-phase microstructure with α -Ti and β -Ti being major and minor constituents, respectively. The intensities of β -Ti peaks seem to be greatly reduced after the specimen is annealed at 800 °C for 5 h, which should be associated with the $\beta \rightarrow \alpha$ transformation. In addition, a comparison

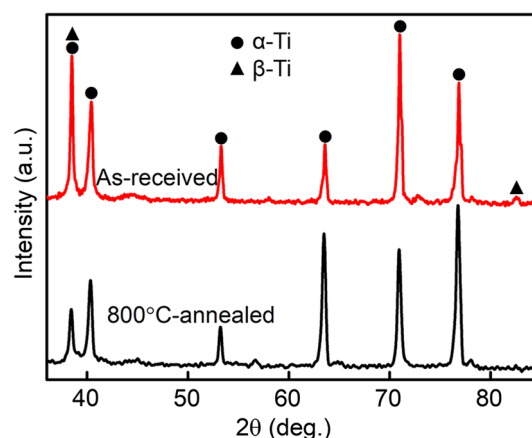


Fig. 1 XRD patterns of the as-received and the 800 °C-annealed specimens

between diffraction characteristics of the α phase in both the specimens reveals remarkable intensity difference for some peaks, suggesting that the specimen texture should have been changed during the annealing treatment.

3.2 ECC and EDS Examinations

Figure 2a, b shows direct microstructural observations of the as-received specimen, respectively. Two types of morphologies can be clearly distinguished - matrix grains (majority) in nearly equiaxed shape and black short-rod phases (minority) uniformly distributed along matrix grain boundaries. They are believed to correspond to the α and the β phases, as suggested by the XRD result (Fig. 1). Specific compositions of the two phases are further measured by the EDS, with results shown in Fig. 3. One can see that the V content of point P2 (corresponding to the short-rod phase) is much higher than that of point P1 (matrix). Previous researches [21–23] revealed that the maximum solubility of V in β -Ti was considerably higher than that in α -Ti. Therefore, the black short-rod phases in Fig. 2a, b can be confirmed to be the V-enriched β phase while the matrix grains correspond to the V-depleted α phase.

ECC images of microstructures of the annealed specimen are presented in Fig. 2c, d, from which remarkable

changes can be noticed. After annealing at 800 °C for 5 h, the matrix grains are found to be evidently coarsened and the prior β phases distributed along α grain boundaries (Fig. 2a) seem to be completely replaced by a type of equiaxed structures. Figure 2d further reveals that a large number of fine plates exist inside the equiaxed structures, with an average value of plate widths measured to be ~ 240 nm. Malinov et al. [24] demonstrated rapid cooling like quenching in cold water was able to trigger martensitic $\beta \rightarrow \alpha$ transformation in TC4 alloy. Considering the suppressed diffraction peaks of the β phase (Fig. 1) in the annealed specimen, the fine plate structures in Fig. 2d are believed to correspond to martensites (α') transformed from grown β phases.

3.3 EBSD Analyses

Figure 4a, b presents EBSD band contrast (BC) and inverse pole figure (IPF) maps (only the α phase indexed) of the as-received specimen, respectively. In the BC map (Fig. 4a), the majority of α grains appear to be fine and uniform. However, the IPF map (Fig. 4b) reveals that only a few out of them belong to recrystallized grains (average size ~ 2.3 μm) surrounded by high angle boundaries (HABs, $\theta > 15^\circ$). Most of the structures correspond to deformed grains elongated along the RD, with a large number of

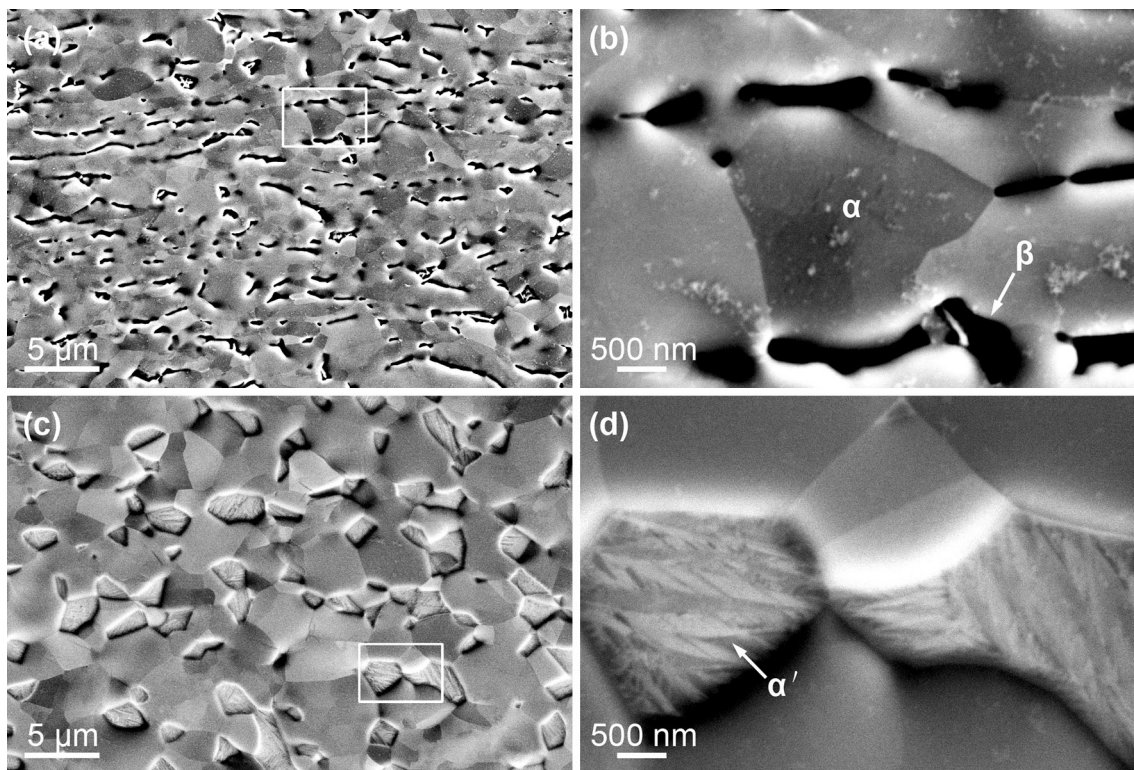


Fig. 2 ECC observations of the as-received **a**, the 800 °C-annealed **c** specimens; white boxes in **a**, **c** are magnified in **b**, **d**, respectively, with different phases labeled

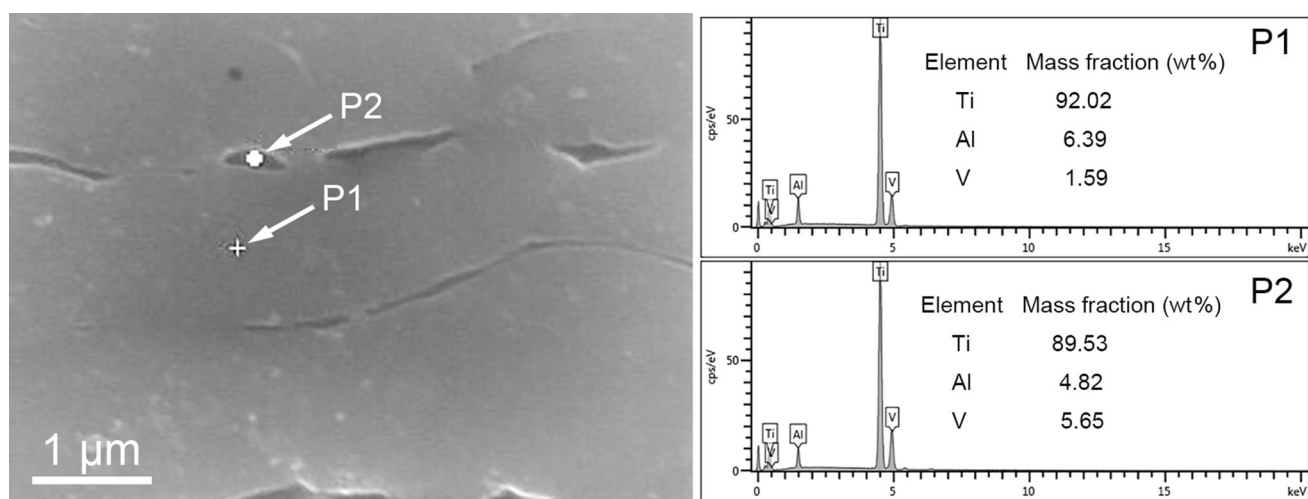


Fig. 3 EDS analyses of the as-received specimen

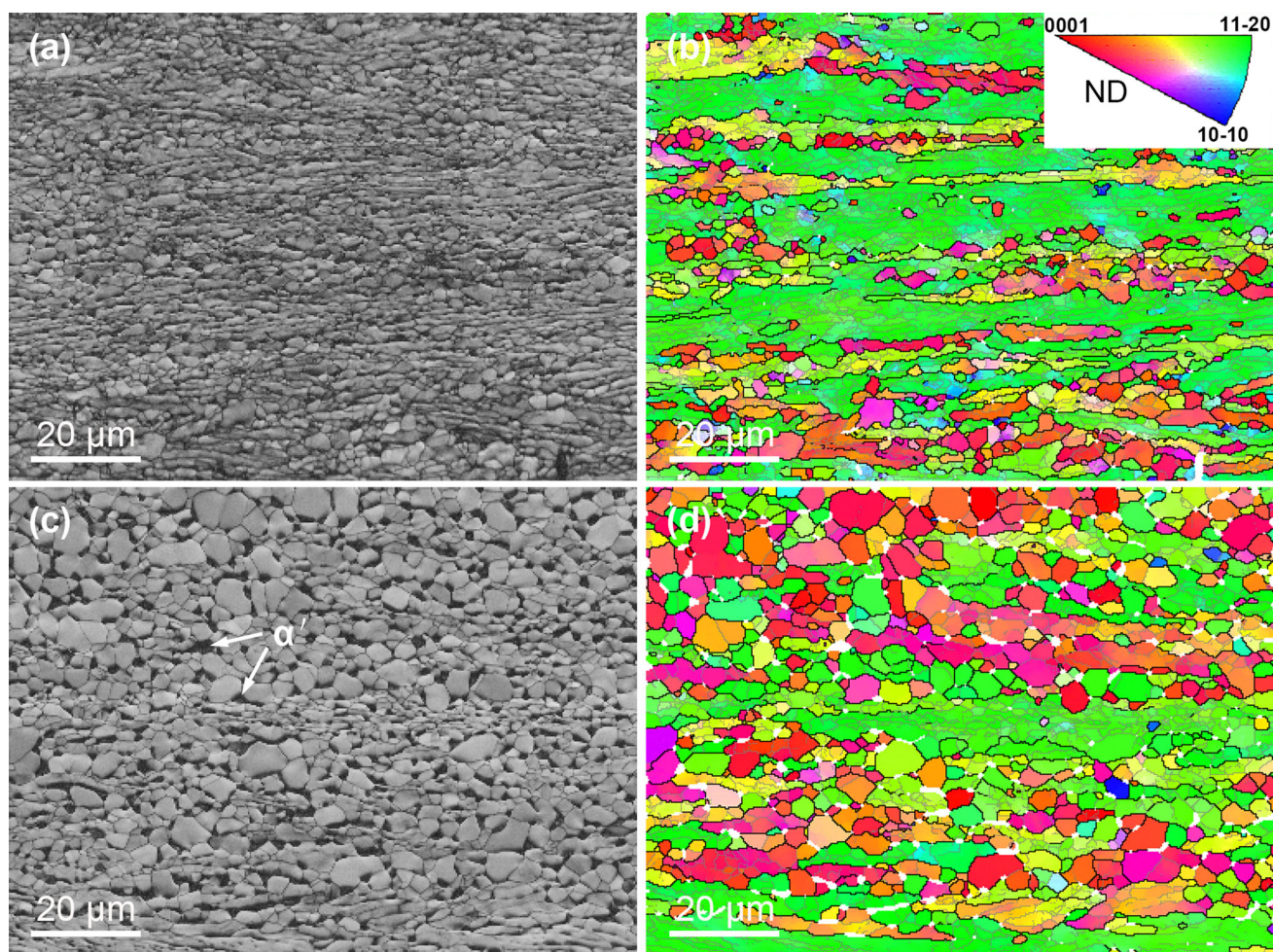


Fig. 4 EBSD characterization: **a** band contrast (BC), **b** inverse pole figure (IPF) maps of the as-received specimen; **c** BC, **d** IPF maps of the 800 °C-annealed specimen. Black and gray lines in **b**, **d** indicate grain boundaries with $\theta > 15^\circ$ and $2^\circ < \theta < 15^\circ$, respectively

subgrains (average size $\sim 1.1 \mu\text{m}$) separating each other by low angle boundaries (LABs, $2^\circ < \theta < 15^\circ$) in their interiors. Also from Fig. 4b, orientations of the un-recrystallized structures are found to be aligned in a similar direction, with grain a -axes concentrated on the ND of the sheet ($\langle 11\text{-}20 \rangle // \text{ND}$). For the recrystallized grains with the well-defined equiaxed shape, however, most grains have their c -axes near the ND of the sheet, showing a completely different orientation feature from that of the un-recrystallized structures. Since hot rolling was experienced by the as-received sheet, the recrystallized grains are believed to result from dynamic recrystallization while dense fine subgrains should be produced by dynamic recovery [22].

For the specimen annealed at 800°C for 5 h, Fig. 4c, d shows that the proportion of well-defined equiaxed grains (recrystallized) is considerably increased along with the occurrence of evident coarsening (average grain size $\sim 3.6 \mu\text{m}$), as compared to the as-received specimen. This suggests that the annealing treatment has promoted the recovered structures to be recrystallized. Nevertheless, there still exist a considerable fraction of un-recrystallized structures which maintain the preferred orientation of $\langle 11\text{-}20 \rangle // \text{ND}$, as shown in Fig. 4d. Due to the evident orientation difference between most recrystallized grains and the un-recrystallized structures, the annealing-induced increase in recrystallized structures could lead to textural modifications, which are better illustrated by comparing their pole figures in the following. Additionally, it is to be noted that black regions dispersed in Fig. 4c (see arrows) should correspond to the martensitic structures in Fig. 2d. They are generally not successfully indexed mainly due to their great fineness and limited spatial resolution of the EBSD technique [25].

Figure 5a, b displays orientation angle distribution histograms of the as-received and the 800°C -annealed specimens, respectively. For the as-received specimen, Fig. 5a shows that the fraction of LABs is evidently higher than

Table 2 Fraction and specific lengths of LABs and HABs corresponding to the EBSD maps in Fig. 4

Microstructural parameters	As-received		800 °C-annealed	
	LABs	HABs	LABs	HABs
Fraction (%)	65.8	34.2	49.4	50.6
Length per area ($1/\mu\text{m}$)	1.01	0.52	0.47	0.47

that of HABs. After the annealing, the fractions of LABs and HABs are decreased and increased, respectively, with the definite statistics presented in Table 2. For both types of boundaries, their boundary lengths per area (specific length) are measured and shown in Table 2. The specific length ($0.47 \mu\text{m}^{-1}$) of LABs in the annealed specimen is found to be much smaller than that ($1.01 \mu\text{m}^{-1}$) of the as-received specimen. As LABs are usually known to be configured by well aligned or slightly tangled dislocations (also called dislocation boundaries), the denser LABs in the as-received specimen suggest a relatively high dislocation density and stored energy [23, 26]. The stored energy should be introduced into the material by the prior hot rolling. The reduced specific length value of LABs indicates that the stored energy is released through the occurrence of recrystallization during annealing at 800°C . In spite of the recrystallization, the specific length value ($0.47 \mu\text{m}^{-1}$) of HABs in the annealed specimen is not increased compared to that ($0.52 \mu\text{m}^{-1}$) of the as-received specimen (Table 2). This indicates that density reduction in HABs due to grain growth may be more significant than generation of new HABs associated with recrystallization nucleation.

Besides, with respect to low misorientation angles ($2^\circ\text{-}8^\circ$) of both the specimens, their rotation axes are also presented in Fig. 5a, b, which indicate strong concentration on the $\langle 0001 \rangle$ direction. Such results allow slip systems activated in both the specimens to be primarily determined.

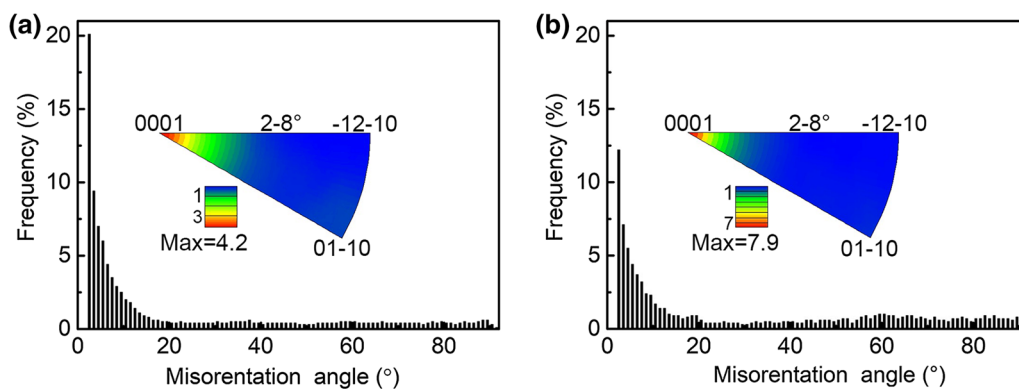


Fig. 5 Misorientation angle and rotation axis distributions of **a** the as-received, **b** the 800°C -annealed specimens

Among all possible slip modes in hcp materials (i.e., prismatic, basal and pyramidal slip), only the prismatic $\langle a \rangle$ slip ($\{10\text{--}10\} \langle 11\text{--}20 \rangle$) provides a lattice rotation around the $\langle 0001 \rangle$ direction [27, 28]. This suggests that the low angle peak in Fig. 5 could be largely attributed to preferential activation of prismatic $\langle a \rangle$ slip during the hot rolling and the annealing. This is also supported by the fact that the prismatic $\langle a \rangle$ slip always possesses the smallest critical resolved shear stresses among various deformation modes in α -Ti [29, 30], making it the easiest one to be initiated.

Figure 6 presents pole figures of the as-received and the annealed specimens. It can be seen from Fig. 6a that c -axes of the predominant majority of grains are aligned toward the TD ($c//TD$), along with preferred orientation characteristics of $\langle 11\text{--}20 \rangle // ND$ and $\langle 10\text{--}10 \rangle // RD$. In fact, such textural features are consistent with the orientation characteristics of the un-recrystallized structures in Fig. 4b (green regions), suggesting the predominance of hot-rolled structures in the as-received specimen. It should be noted that the $\{0001\}$ pole figure in Fig. 6a also reveals a small number of orientations with their c -axes deviated from the TD. They are further extracted (the white circled regions in Fig. 6a) and recalculated in Fig. 6b. Accordingly, grain morphologies corresponding to such orientations are presented in Fig. 6c. One can notice that the extracted grains are essentially those recrystallized grains revealed in Fig. 4b, with their c -axes tilted about $\pm 20^\circ$ from the ND toward the RD.

For the annealed specimen, although its major textural feature ($c//TD$, $\langle 11\text{--}20 \rangle // ND$ and $\langle 10\text{--}10 \rangle // RD$), as shown in Fig. 6d) is quite similar to that of the as-received specimen, the maximum texture intensity is found to be greatly reduced from 33.5 to 17.9. Similarly, extraction and re-analyses are performed for orientations with c -axes deviated from TD, i.e., those white circled in Fig. 6d. Their recalculated $\{0001\}$ pole figure and grain morphologies are displayed in Fig. 6e, f, respectively. Also, the extracted orientations are found to essentially correspond to the recrystallized grains in the annealed specimen. Noticeably, the textural intensity of the recrystallized grains in the annealed specimen is evidently higher than that of the as-received specimen, suggesting that further intensified orientation preference can be induced for the concentrated recrystallized structures by the annealing. Meanwhile, a further comparison between Fig. 6b, e reveals that the preferred orientations of the recrystallized structures are shifted toward the TD after annealing, slightly different from those of the as-received specimen. This indicates that new orientations have been intensively generated through recrystallization nucleation and/or preferred growth of specific grains has occurred during the annealing. As a result of the increase in recrystallized structures at the

expense of deformed/recovered structures, the global texture of the TC4 specimen is weakened by the annealing treatment.

Note that textural evolution during annealing has also been investigated for single-phase α -Ti alloys in recent years. Distinct from the $c//TD$ textural feature in rolled dual-phase Ti alloys (for example Fig. 6a), a bimodal basal texture (c -axes inclined about $\pm 30^\circ$ from the ND toward the TD) is usually observed for commonly rolled α -Ti alloys [31, 32]. In addition, very limited textural changes can be noted for α -Ti alloys during insufficient recrystallization annealing [31], different from the evident textural weakening for the annealed TC4 (Fig. 6). In-depth reasons accounting for such a difference are still unclear and should be well explored in future work.

3.4 Hardness Measurements

Hardnesses of both the as-received and the annealed specimens are measured and shown in Fig. 7. Compared to the hardness (367.0 HV on average) of the as-received specimen, the annealed specimen has a lower average value of 320.5 HV, suggesting a $\sim 12.7\%$ drop. Such a hardness change must be related to the annealing-induced microstructural and textural changes as above illustrated. The decreased hardness could be mainly attributed to several factors. First of all, the increased sizes of recrystallized grains after annealing could soften the material due to the Hall–Petch effect, which can be approximated using the following equation,

$$\Delta HV = k_{HV} (d_1^{-0.5} - d_0^{-0.5}), \quad (1)$$

where ΔHV is the hardness change, k_{HV} is the Hall–Petch slope in the unit of Vickers hardness ($80 \text{ HV } \mu\text{m}^{1/2}$ for α -Ti [33]), d_0 and d_1 are average grain sizes of the as-received ($\sim 2.3 \mu\text{m}$) and the annealed ($\sim 3.6 \mu\text{m}$) specimens. The ΔHV calculated according to Eq. (1) is -10.5 HV , accounting for only a small part of the hardness drop ($320.5 - 367.0 = -46.5 \text{ HV}$) in Fig. 6.

The second important factor points to the effective release of stored energy that would reduce the dislocation and LABs densities, leading to lowered deformation resistance [34]. A third softening contributor may be the weakened texture that include more soft orientations, allowing more slip and/or twinning modes to be activated during deformation. Nevertheless, it is to be noted that the stress state during hardness test is much more complex than that during uniaxial tension or compression. As a result, more deformation modes could be initiated during the hardness test of hcp metals, leading to suppressed hardness anisotropy as demonstrated in a recent work [35]. This

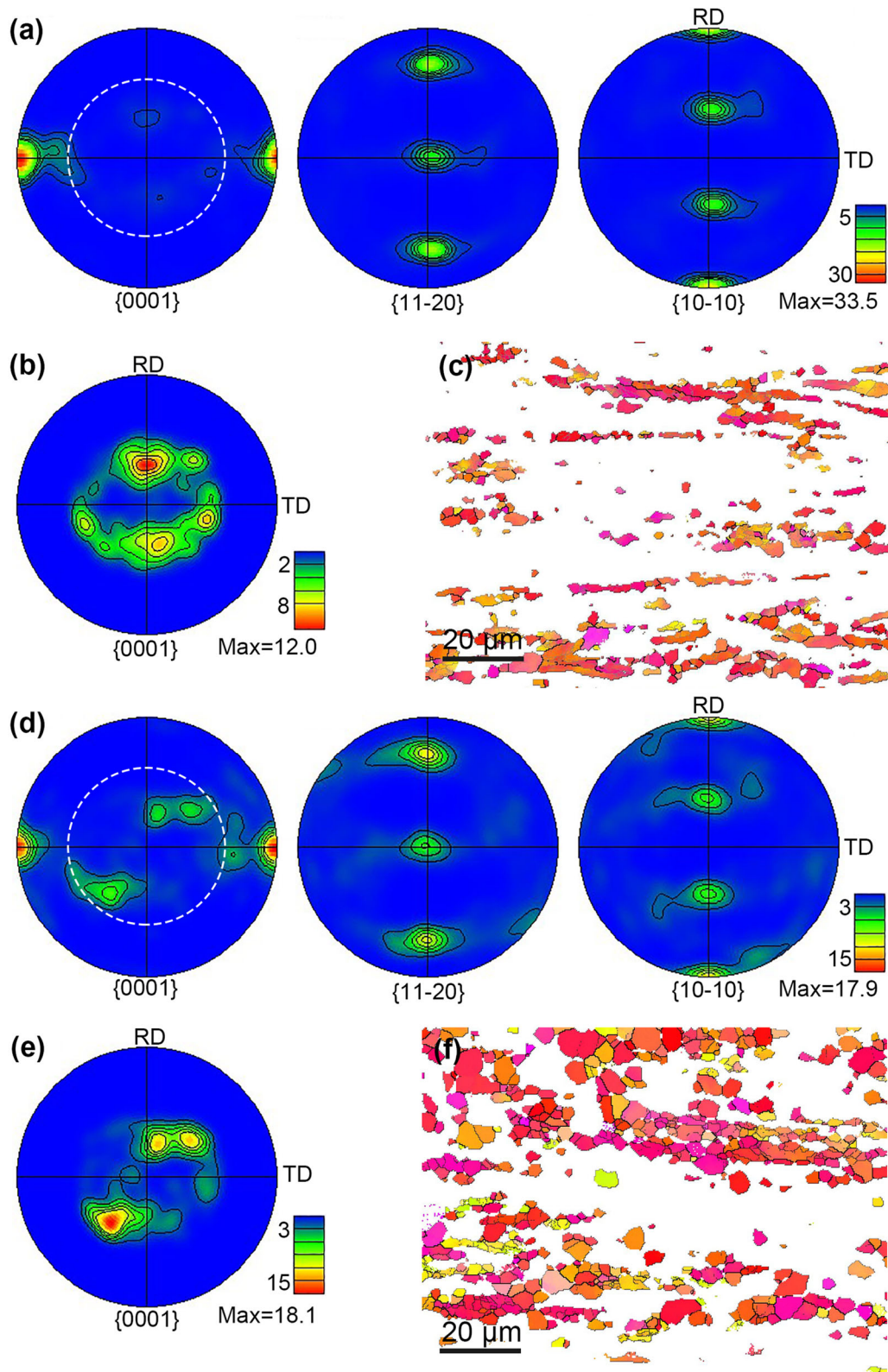


Fig. 6 Pole figures of **a** the as-received, **d** the 800 °C-annealed specimens; **b**, **e** recalculated pole figures for the circled orientations in **a**, **d**, respectively; **c**, **f** IPF maps corresponding to **b**, **e**, respectively

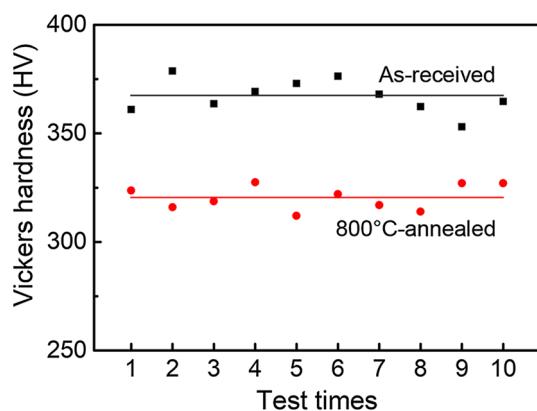


Fig. 7 Hardness variations of the specimens before and after annealing

means that hardening/softening contribution from texture may not be pronounced in the present work.

In addition, it is to be noted that the $\beta \rightarrow \alpha$ martensitic transformation has been induced by cooling in water immediately after the annealing at 800 °C, giving birth to fine α' plates as revealed in Fig. 2d. In contrast with the above factors leading to softening, such fine martensitic plates are generally known to be hardening contributors [36, 37]. In the present case, however, the coexistence of multiple softening factors seems to fully offset the hardening effect of such martensites. Nevertheless, the relatively mild hardness drop ($\sim 12.7\%$) in the annealed specimen suggests that they have indeed contributed to the specimen hardness.

4 Conclusions

- (1) The as-received hot-rolled TC4 sheet has a typical dual-phase ($\alpha + \beta$) microstructure, with the α -Ti as the major phase and short-rod β -Ti (minority) uniformly distributed throughout the α matrix. Most of α grains correspond to the un-recrystallized structures (dense LABs in their interiors) with a typical rolling texture ($c//TD$ and $\langle 11\text{--}20 \rangle // ND$).
- (2) After the annealing at 800 °C for 5 h, the stored energy and LABs density in the as-received specimen are significantly reduced, along with the occurrence of recrystallization and grain growth that weaken the initial texture.
- (3) Martensitic transformation is induced by water quenching immediately after the annealing, allowing the high-temperature β phases to be transformed into submicron α plates.
- (4) The hardness of the annealed specimen is 320.5 HV, lower than that (367.0 HV) of the as-received specimen, which could be mainly attributed to

reduced LABs, grain growth and weakened texture. Nevertheless, the hardening effect from the fine martensitic plates could help to suppress a drastic hardness drop.

Acknowledgements This work was supported by the Fundamental and Cutting-Edge Research Plan of Chongqing (cstc2017jcyjAX0114 and cstc2015jcyjBX0048), the Scientific and Technological Research Program of Chongqing Municipal Education Commission (KJ1600924) and the Education Reform Project for Professional Degree Graduate of Chongqing University of Technology (ZSSD103).

References

- [1] P. Singh, H. Pungotra, N.S. Kalsi, *Mater. Today Proc.* **4**, 8971 (2017)
- [2] D. Banerjee, J.C. Williams, *Acta Mater.* **61**, 844 (2013)
- [3] R.R. Boyer, *Mater. Sci. Eng. A* **213**, 103 (1996)
- [4] S. Dai, Y. Wang, F. Chen, *Mater. Charact.* **104**, 16 (2015)
- [5] M. Peters, J. Kumpfert, C.H. Ward, C. Leyens, *Adv. Eng. Mater.* **5**, 419 (2003)
- [6] P. Guo, Y. Zhao, W. Zeng, *Rare Met. Mater. Eng.* **44**, 277 (2015)
- [7] F.J. Gil, M.P. Ginebra, J.M. Manero, J.A. Planell, *J. Alloys Compd.* **329**, 142 (2001)
- [8] L. Zeng, T.R. Bieler, *Mater. Sci. Eng. A* **392**, 403 (2005)
- [9] T. Fang, W. Wang, *Mater. Chem. Phys.* **56**, 35 (1998)
- [10] P. Guo, Y. Zhao, W. Zeng, Q. Hong, *Mater. Sci. Eng. A* **563**, 106 (2013)
- [11] G. Lütjering, *Mater. Sci. Eng. A* **243**, 32 (1998)
- [12] S. Sun, Y. Zong, D. Shan, B. Guo, *Trans. Nonferr. Met. Soc. China* **20**, 2181 (2010)
- [13] X. Peng, H. Guo, T. Wang, Z. Yao, *Mater. Sci. Eng. A* **533**, 55 (2012)
- [14] S. Wang, X. Wu, *Mater. Des.* **36**, 663 (2012)
- [15] N. Bozzolo, N. Dewobroto, T. Grosdidier, P. Barb eris, F. Wagner, *Mater. Sci. Forum* **467–470**, 441 (2004)
- [16] N. Kherrouba, M. Bouabdallah, R. Badji, D. Carron, M. Amir, *Mater. Chem. Phys.* **181**, 462 (2016)
- [17] M. Yang, G. Wang, T. Liu, W.J. Zhao, D.S. Xu, *Acta Metall. Sin. (Engl. Lett.)* **30**, 745 (2017)
- [18] T. Karthikeyan, A. Dasgupta, R. Khatirkar, S. Saroja, I. Samajdar, M. Vijayalakshmi, *Mater. Sci. Eng. A* **528**, 549 (2010)
- [19] G.C. Obasi, S. Biroasca, J. Quinta Da Fonseca, M. Preuss, *Acta Mater.* **60**, 1048 (2012)
- [20] S.A. Souza, R.B. Manicardi, P.L. Ferrandini, C.R.M. Afonso, A.J. Ramirez, R. Caram, *J. Alloys Compd.* **504**, 330 (2010)
- [21] T. Ahmed, H.J. Rack, *Mater. Sci. Eng. A* **243**, 206 (1998)
- [22] Y. Ning, B. Xie, H. Liang, H. Li, X. Yang, H. Guo, *Mater. Des.* **71**, 68 (2015)
- [23] H. Liu, K. Nakata, J. Zhang, N. Yamamoto, J. Liao, *Mater. Charact.* **65**, 1 (2012)
- [24] S. Malinov, W. Sha, Z. Guo, C. Tang, A. Long, *Mater. Charact.* **48**, 279 (2002)
- [25] A.C. Lewis, S. Wright, *JOM* **65**, 1221 (2013)
- [26] L. Chai, S. Wang, B. Luan, Q. Liu, *Sci. China Technol. Sci.* **59**, 673 (2016)
- [27] Y.B. Chun, M. Battaini, C.H.J. Davies, S.K. Hwang, *Metall. Mater. Trans. A* **41**, 3473 (2010)

- [28] G.S. Dyakonov, S. Mironov, S.V. Zherebtsov, S.P. Malysheva, G.A. Salishchev, A.A. Salem, S.L. Semiatin, *Mater. Sci. Eng. A* **607**, 145 (2014)
- [29] F. Bridier, D.L. McDowell, P. Villechaise, J. Mendez, *Int. J. Plast.* **25**, 1066 (2009)
- [30] M. Zhang, F. Bridier, P. Villechaise, J. Mendez, D.L. McDowell, *Acta Mater.* **58**, 1087 (2010)
- [31] S. Wronski, M. Jedrychowski, J. Tarasiuk, B. Bacroix, *Mater. Sci. Eng. A* **692**, 113 (2017)
- [32] Y. Wang, W. He, N. Liu, A. Chapuis, B. Luan, Q. Liu, *Mater. Charact.* **136**, 1 (2018)
- [33] L. Chai, H. Wu, Z. Zheng, H. Guan, H. Pan, N. Guo, B. Song, *J. Alloys Compd.* **741**, 116 (2018)
- [34] P. Luo, D.T. McDonald, W. Xu, S. Palanisamy, M.S. Dargusch, K. Xia, *Scr. Mater.* **66**, 785 (2012)
- [35] F. Guo, H. Yu, C. Wu, Y. Xin, C. He, Q. Liu, *Sci. Rep.* **7**, 8647 (2017)
- [36] X. Gao, L. Zhang, J. Liu, J. Zhang, *Mater. Sci. Eng. A* **559**, 14 (2013)
- [37] Z. Tarzimoghadam, S. Sandlöbes, K.G. Pradeep, D. Raabe, *Acta Mater.* **97**, 291 (2015)